

Orientation Dependence of the Elastocaloric Effect in $\text{Ni}_{54}\text{Fe}_{19}\text{Ga}_{27}$ Ferromagnetic Shape Memory Alloy

Nickolaus M. Bruno, Ibrahim Karaman,* and Yuriy I. Chumlyakov

The crystallographic anisotropy of elastocaloric effect (ECE) and relative cooling power (RCP) in $\text{Ni}_{54}\text{Fe}_{19}\text{Ga}_{27}$ shape memory alloy single crystals are studied via compression tests. Single crystals are studied along the [001], [123], and [011] austenite directions and yield different ECE behaviors and maximum RCPs for various strain levels. A thermodynamic framework using the Helmholtz free energy is employed to analyze the total entropy change as a function of strain. Thermodynamic losses are computed from the mechanical hysteresis of superelasticity experiments to quantify the strain dependent RCP. It is found that the [001] orientation generates the highest maximal RCP of 738 J kg^{-1} when unloaded from 200 MPa. This is attributed mainly to the large superelastic temperature window of 45 K. However, loading the crystals to stresses higher than 200 MPa causes a multistep transformation in the [011] direction, thus reducing the alloy's overall RCP by 135 J kg^{-1} . This is a consequence of the negative entropy change and large transformation hysteresis generated by the second-stage transformation in the [011] direction. Interestingly, if only the first-stage transformation in [011] is employed for the ECE, the [011] direction yields the highest RCP compared to [001] and [123] for any strain up to 3.5%.

are capable of converting applied magnetic energy, hydrostatic pressure, and mechanical energy to thermal energy through a two-way coupling giving rise to the giant magnetocaloric,^[6–16] barocaloric,^[16–18] and elastocaloric^[19–22] effects. These effects can be measured in both austenite (high temperature) and martensite (low temperature) phases, independently, as well as from the latent heat produced by the reversible transformation between the two.

Until recently, most of the work involving the caloric behavior of SMAs has been focused on the magnetocaloric effect (MCE) in magnetic SMAs (MSMAs).^[6–16] The MCE in MSMAs requires large magnetic driving forces from magnetic fields greater than 2 T to achieve reversible temperature changes that are comparable with those of other non-MSMA solid-state rare-earth refrigerants, example Gd. In normal MCE operations, bulky superconducting magnets are needed to produce the magnetic fields^[23] large enough to drive the martensitic transformation. Here, the giant elastocaloric effect (ECE) defined by the stress-induced entropy

change was studied in SMAs offering an additional magnetic field-free method of driving temperature changes applicable to solid state refrigeration. This caloric effect is specific to SMAs that exhibit reversible stress-induced martensitic transformation.

Although the giant ECE has been known of for some time,^[19–22] there is a lack of available scientific data needed for the successful design and implementation, or optimization, of multicomponent ECE systems. SMAs have been studied for their giant ECE via stress-induced martensitic transformation and include NiTi,^[19] NiFeGa,^[24,25] CuZnAl,^[22,26] NiMnGaFe,^[27] NiMnGaCo,^[28] NiMnSn(Cu),^[29] and NiCoMnIn.^[21] These alloys have been reported to exhibit stress-induced isothermal entropy changes of around 30, 10–20, 22.8, 5.5, 2.5, 1.75, and $5.5 \text{ J kg}^{-1} \text{ K}^{-1}$ under the stresses of 500, 150, 105, 9.3, 9.8, 5.24, and 75 MPa, respectively. Unlike non-transforming solid ECE materials, SMAs have enhanced ECE due to the larger entropy change, ΔS , originating from the martensitic phase transformation. Usually, the above alloys were characterized by a total transformation entropy change from martensite, M , to austenite, A , $\Delta S^{M \rightarrow A}$, of around $20 \text{ J kg}^{-1} \text{ K}^{-1}$ or less. This entropy change usually corresponds to an adiabatic temperature change of around 5 K. In few of the latter studies mentioned above, only part of the transformation entropy change was accessed under the applied mechanical loads due to inherent sample brittleness in polycrystals, or other


1. Introduction

Over the past few decades, materials exhibiting giant recoverable strain, entropy changes, and change in physical properties by means of a reversible phase transformation have drawn considerable scientific attention. These materials include shape memory alloys (SMAs) which are thought to be ideal candidates for high precision thermo-mechanical actuators^[1–3] due to their ability to convert thermal energy into large recoverable strains through the shape memory effect.^[4,5] It has also been shown that some SMAs

Dr. N. M. Bruno, Prof. I. Karaman
Department of Materials Science and Engineering
Texas A&M University, College Station, TX 77843, USA
E-mail: ikaraman@tamu.edu

Dr. N. M. Bruno
Department of Mechanical Engineering, South Dakota School
of Mines and Technology, Rapid City, SD 57701, USA

Prof. Y. I. Chumlyakov
Siberian Physical Technical Institute, Tomsk State University
Tomsk 634050, Russia

 The ORCID identification number(s) for the author(s) of this article can be found under <https://doi.org/10.1002/pssb.201700437>.

DOI: 10.1002/pssb.201700437

experimental limitations including the inability to apply large mechanical loads.

In the present study, the ECE of the single crystalline off-stoichiometric Heusler alloy $\text{Ni}_{54}\text{Fe}_{19}\text{Ga}_{27}$ (at.%) was indirectly quantified under compressive loading along the [001], [123], and [011] crystallographic directions of the austenite phase. This particular alloy composition was selected because it exhibited a stable and repeatable superelastic behavior along the [001] and [123] crystallographic directions and a multi-step transformation along the [011] direction.^[30–32] This particular alloy is free of Mn, which is beneficial to manufacturing the alloy and for the compositional control during melting. Typically, Mn containing SMAs pose manufacturing difficulties due to the high volatility of Mn and compositional sensitivity to the superelastic behavior. Furthermore, NiFeGa single crystals have been shown to exhibit large crystalline anisotropy,^[33–38] that is, austenite crystal directions are characterized by different transformation stress hysteresis, $\Delta\sigma_{\text{hys}}$, moduli of elasticity, E_A , coefficients of thermal expansion, α , transformation strain, ε_{tr} , and critical stress versus temperature phase diagram slopes, $d\sigma/dT$, along different austenite crystallographic orientations. Studying single crystals along different crystallographic orientations was expected to provide a means to identify some key materials parameters that facilitate in understanding how to enhance the ECE in SMAs without introducing ambiguity from the mechanical effects of neighboring grains.

To compute the ECE here, a thermodynamic Maxwell Relation was derived from the Helmholtz free energy potential. Superelastic stress–strain data was then analyzed using the Maxwell Relation. The assumptions employed in deriving the Maxwell Relation served as the boundary conditions for the isothermal compression experiments. The Helmholtz free energy potential was derived from a material's free energy assuming an isochoric transformation. Conventionally, the Gibbs free energy expression is employed to quantify the caloric effects in SMAs under the premise that an isobaric transformation has taken place. In terms of stress-induced entropy changes, the Maxwell Relation could not be developed from the Gibbs free energy potential. Therefore, the Helmholtz free energy potential was employed.

2. Experimental Procedures

2.1. Material Fabrication

The $\text{Ni}_{54}\text{Fe}_{19}\text{Ga}_{27}$ (at.%) single crystals were fabricated using the Bridgman technique in a high purity He atmosphere. In the as-grown state, the crystals had a single phase structure without any ductile γ phase^[30,39] precipitates, verified by scanning electron microscopy (SEM). The composition of the crystals was verified using a CAMECA SX-50 electron microprobe equipped with a multi-crystal wavelength dispersive X-ray spectrometer (WDS). Electro-discharge machining (EDM) was employed to cut compression specimens of $4 \times 4 \times 8 \text{ mm}^3$ so that the longitudinal direction corresponded to the crystallographic compression directions mentioned earlier. Crystallographic loading directions (specimen longitudinal axis) were verified by diffracting the compression surface using Cu K_α X-rays in a Bruker D8 X-ray diffractometer and verifying the location (in 2θ) of the diffraction peaks.

To determine stress-free martensitic transformation temperatures, a 4 mm diameter, 2 mm thick specimen was subjected to calorimetry at a heating/cooling rate of 10 K min^{-1} in a TA Instruments Q20 Differential Scanning Calorimeter (DSC). The transformation temperatures, i.e., the martensite finish (M_f) and start (M_s), as well as the austenite start (A_s) and finish (A_f) temperatures, were extracted from the DSC thermograms using the conventional double tangents method and were determined to be 275, 280, 284, and 288 K, respectively.

2.2. Thermo-Mechanical Characterization

2.2.1. Characterization of Isothermal Superelasticity

Single crystals with longitudinal loading directions corresponding to each of the three austenite crystal directions, i.e., [001], [123], and [011], were characterized using a custom thermo-mechanical test setup consisting of a screw-driven mechanical testing system, PID temperature controllers, electric heaters, and liquid nitrogen cooling channels. The NiFeGa single crystals were installed into the testing stage and the temperature was controlled through conduction with the surrounding hardware similar to the setup described in Ref. ^[40].

Isothermal compression tests were performed under quasi-static displacement control (corresponding to $0.06\% \varepsilon \text{ sec}^{-1}$) to prevent temperature fluctuations resulting from the stress-induced latent heat of the structural transformation. Despite the slow strain rate, temperature fluctuations of approximately 0.4 K were measured during the mechanical loading and unloading which were attributed to the observed burst-type martensitic transformation that occurred after sufficient mechanical loads were applied and thermocouple error. This temperature uncertainty was employed to compute error bars for the entropy change data.

Compressive strain was measured using an MTS high temperature extensometer (HTEX) with ceramic tips lightly pressed against the top and bottom compression rods with a spring mechanism. Specimen surface temperature was actively measured along its lateral surface every one second during the mechanical loading using a spring loaded thermocouple. The specimen and compression rods were insulated using pyrogel to prevent heat leaks to the surroundings. The stress–strain ($\sigma - \varepsilon$) response was measured with the same acquisition rate (1 Hz) as temperature so that σ , ε , and temperature, T , could be compared at the same $\sigma - \varepsilon$ instant in time.

2.2.2. Isothermal Entropy Change

Stress–strain–temperature ($\sigma - \varepsilon - T$) data were measured and then used to compute the total entropy change across the stress-induced transformation in the [001], [123], and [011] austenite loading directions. Isothermal superelastic loading was performed from 253 to 353 K in increasing increments of about 3 K. Since each sample was initially at room temperature before the start of testing and then cooled to 253 K (below M_f), a mechanical load of 3000 N was applied to each sample upon reaching 253 K to reorient the self-accommodated martensite, that formed upon

cooling, to its stress-preferred orientation. This martensitic reorientation was assumed to not create a large entropy (or temperature) change because no phase transformation was triggered by applying the load to the already temperature-stabilized martensite.

After the initial reorientation of self-accommodated martensite, a constant 5–10 MPa preload was left on the sample during the discontinuous heating sequence,^[41] thus allowing the compression rods to conduct heat to the sample as the sample continually changed dimension through thermal expansion. Once the sample reached the test temperature on heating, a large mechanical load, which will be identified later, was again applied and removed to generate the superelastic response. This discontinuous heating protocol for the elasto-caloric measurement, here, is the equivalent experimental procedure to that followed by the magneto-caloric measurements in the literature^[41,42] with the addition of reorienting the self-accommodated martensite to its stress-preferred orientation.

Isothermal stress–strain data was then processed using a discretized form of the Maxwell Relation, mentioned earlier, that was derived from the Helmholtz free energy potential for isochoric transformations.^[43] The Helmholtz free energy potential, ψ , was defined as:

$$\psi = U - TS, \quad (1)$$

where U is the SMA's free energy, T is temperature, and S is total entropy. The change in ψ was computed with implicit differentiation as:

$$d\psi = dU - SdT - TdS, \quad (2)$$

where dU is the change in internal energy which depended on added heat, dQ , and the work done by the system, dW' .

$$dU = dQ + dW', \quad (3)$$

through the second law of thermodynamics, $dQ = TdS$, and all other extensive (volume dependent) work terms were represented as dW' . In the case of uniaxial mechanical loading experiments, the compression sample was characterized by volume, magnetization, and uniaxial strain in the direction of the stress. The change in applicable work terms was denoted as:

$$dW' = -PdV + \frac{\sigma d\varepsilon}{\rho} + HdM. \quad (4)$$

In Equation (4), P is hydrostatic pressure on the specimen control volume, V , σ is uniaxial stress, ε is uniaxial strain, ρ is mass density (7803 kg m^{-3}), H is an applied magnetic field, and M is specimen magnetization. The PdV term is negative by convention. In the superelastic stress–strain experiments in this study, the volume was assumed to be constant, as the volume change between austenite and martensite in most SMAs is negligibly small. Furthermore, the specimen magnetization did not change as no magnetic field was applied during experimentation. Therefore, the change in internal energy, dU , during superelastic experiments reduced to

$$dU = \frac{\sigma d\varepsilon}{\rho} - TdS. \quad (5)$$

Substituting Eq. (5) into Eq. (2), the Helmholtz free energy potential reduced to

$$d\psi = \frac{\sigma d\varepsilon}{\rho} - SdT, \quad (6)$$

according to Eq. (6) the total entropy of the SMA was computed for constant strain, i.e., $d\varepsilon = 0$ as

$$-S = \frac{d\psi}{dT}, \quad (7)$$

and the stress on the SMA's control volume was computed assuming the temperature was constant, i.e., $dT = 0$ as

$$\frac{\sigma}{\rho} = \frac{d\psi}{d\varepsilon}. \quad (8)$$

The Maxwell relation was then derived by equating the derivative of Eq. (7) with respect to the independent variable in Eq. (8), with the derivative of Eq. (8) with respect to the independent variable in Eq. (7). Thus,

$$-\frac{dS}{d\varepsilon} = \frac{d}{d\varepsilon} \left(\frac{d\psi}{dT} \right) = \frac{1}{\rho} \frac{d\sigma}{dT} = \frac{d}{dT} \left(\frac{d\psi}{d\varepsilon} \right) \quad (9)$$

or

$$-\frac{dS}{d\varepsilon} = \frac{1}{\rho} \frac{d\sigma}{dT}, \quad (10)$$

naturally, this was reduced and expressed in integral form to describe the elasto-caloric effect (ECE),

$$-dS = \frac{1}{\rho} \frac{d\sigma}{dT} d\varepsilon \Rightarrow -\Delta S = \frac{1}{\rho} \int_0^\varepsilon \frac{d\sigma}{dT} d\varepsilon. \quad (11)$$

Equation (11) parallels much of what was reported in the literature for the study of the magneto-caloric effect (MCE), however, the MCE is typically derived from the Maxwell Relation of Gibbs free energy. The Gibbs free energy is derived under isobaric, or constant stress, assumptions, and, therefore, for ECE experimentation, the most accurate method is to use the Helmholtz free energy.

Despite the fact that we used Helmholtz free energy to develop the Maxwell Relation, Eq. (11) was technically not a valid approach to quantify the giant ECE from stress–strain data across first-order phase transformations.^[44] This is due to the apparent discontinuous behavior in $\sigma - T$ at the point of the structural phase change from austenite (martensite) to martensite (austenite). Recently, however, many reports aimed to endorse the applicability of a discrete form of Eq. (11) applied across first order transitions to quantify multi-caloric behavior in SMAs.^[41,44–46] Since results have been validated in

numerous reports that employ this method for MCE studies, we also employed it, herein, to quantify the ECE from superelastic loading curves.

The discrete form of Eq. (11) paralleled that of studies of the MCE^[41,46] in SMAs and was denoted as:

$$-\Delta S(T_K, 0 \rightarrow \varepsilon) = \frac{1}{\rho \Delta T} \left[\int_0^\varepsilon \sigma_{T_{k+1}} d\varepsilon - \int_0^\varepsilon \sigma_{T_k} d\varepsilon \right], \quad (12)$$

where T_{k+1} and T_k are isothermal test temperatures, $T_{k+1} > T_k$, $\Delta T = T_{k+1} - T_k$, and $T_K = (T_{k+1} + T_k)/2$.

This formula was applied to the superelastic loading/unloading curves of NiFeGa single crystals and the limits of integration were reversed to determine the ECE entropy change on mechanical unloading. Conceptually, the latter implies that the initial condition of the SMA during ECE experimentation was the stress induced and fully compressed (stress-preferred) martensite phase.

3. Results and Discussion

3.1. Isothermal Superelastic Response

Figure 1 shows the superelastic response at the A_f temperature (288 K) the [011] austenite loading direction and the [001] and [123] in the inset. Upon mechanical loading at this temperature, following the linear elastic response of the austenite phase, the stress-induced martensite transformation took place. After the martensitic transformation was completed with sufficient loading, the linear elastic response of martensite was evident in the stress–strain responses. Complete superelasticity (SE) was observed in each direction as the mechanical load was removed, as depicted in the figure. As shown in the inset, the [001]

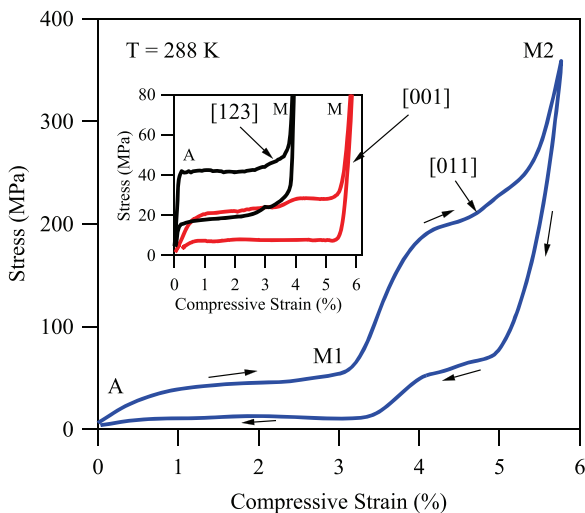


Figure 1. The compressive stress – uniaxial strain response of the [001], [123], and [011] austenite crystal directions in Ni₅₄Fe₁₉Ga₂₇ shape memory alloy at the A_f temperature (288 K). A denotes the austenite phase and M denotes martensite. M1 and M2 represent the 14M and L1₀ austenite phases of the [011] loading direction, respectively.

direction started to transform from austenite to martensite (σ^{M_s}) at 19.4 MPa and the [123] direction at 41.8 MPa. Each of the stress induced transformations finished at stresses of 29.4 and 51.0 MPa, respectively. Preliminary experimentation was performed up to 300 MPa, but data is only shown up to 80 MPa for clarity of mechanical hysteresis loops and critical stresses.

On the other hand, loading along the [011] direction produced a multistep stress-induced martensitic transformation starting the first (L2₁ austenite-to-14M martensite, i.e., Martensite 1) around 35 MPa and the second (14M martensite to L1₀ martensite, i.e., Martensite 2^[47,48]) around 200 MPa. Each transformation finished at 56.3 and 262.6 MPa, respectively, as shown in the figure.

The austenite to martensite (forward) transformation was responsible for exothermic heating in the SMAs while the reverse transformation was responsible for the endothermic cooling, or the ECE of interest. Therefore, the unloading curves offered the most relevant stress–strain data for analyzing the cooling ECE in NiFeGa single crystals. Upon unloading, the reverse transformation occurred at around 8.2 MPa along the [001] direction and at 35.1 MPa along the [123] direction. The multistep reverse transformation in the [011] direction occurred from Martensite 2 to Martensite 1 at 74.7 MPa and Martensite 1 to austenite at 13.3 MPa. The difference between the forward and reverse critical stresses for each stress-induced transformation was defined, here, as mechanical hysteresis, or $\Delta\sigma_{\text{hys}}$, which has been listed in **Table 1** for the curves in **Figure 1** at the A_f temperature.

At first glance, the variation in stress hysteresis between the samples was notable and significantly more stress was needed to drive the M1 to M2 transformation in the [011]. If the applied stress exceeded 200 MPa on the [001] and [123] direction a majority of the stress–strain curve would simply be the linear elastic response of martensite, i.e., a single phase generating minimal elastocaloric effect. Therefore, to keep analysis consistent between the different loading directions, the SMA single crystals were loaded up to 200 MPa which had added benefits in the [011] ECE behavior discussed later.

Figure 2a–c depict the superelastic responses of NiFeGa single crystals in the three loading directions up to 200 MPa in compression. Critical stresses for the start and finish of the stress-induced transformation, i.e., martensite start, σ^{M_s} , martensite finish, σ^{M_f} , austenite start, σ^{A_s} , austenite finish, σ^{A_f} have been labeled on a couple of the stress–strain curves for clarity. Furthermore, the area of the stress hysteresis, which indicates

Table 1. The transformation strain (ε_{tr}) at the test temperature A_f , stress hysteresis at A_f , and elastic modulus of the austenite phase for the [001], [123], and [011] crystallographic directions in the single crystalline Ni₅₄Fe₁₉Ga₂₇ shape memory alloy under compression.

Crystal direction	$\Delta\sigma_{\text{hys}} _{T=A_f}$ (MPa)	ε_{tr} (%)	E_A (GPa)
[001]	16	4.9	7.4
[123]	22	3.1	17
[011]	32 ^{a)}	3.0 ^{a)}	17
	145 ^{b)}	1.8 ^{b)}	

^{a)} First stage martensitic transformation (L2₁ to 14M martensite);

^{b)} Second stage martensitic transformation (14M to L1₀ martensite).

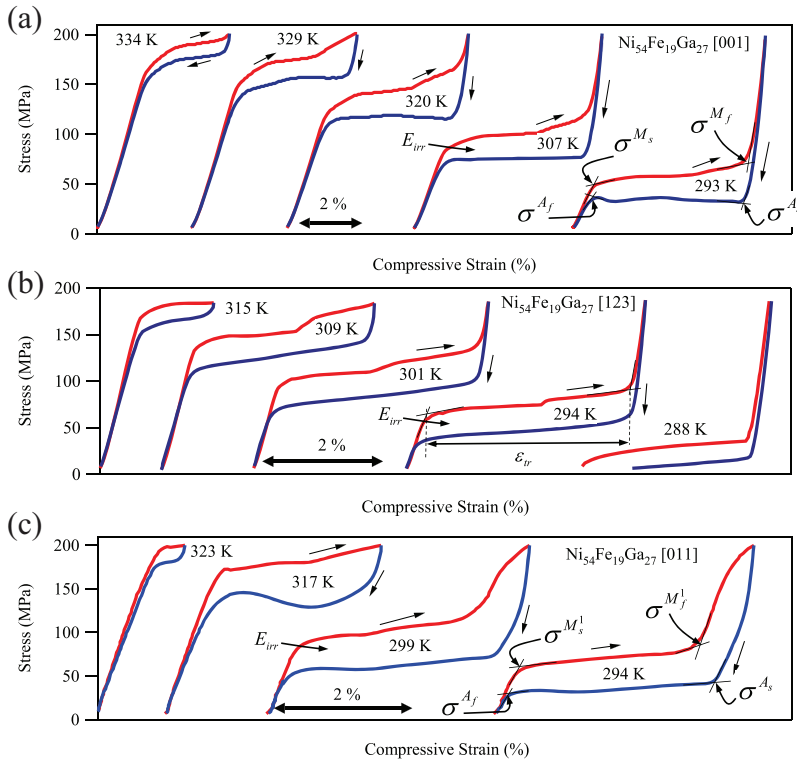


Figure 2. Isothermal compressive stress – uniaxial strain responses of the (a) [001], (b) [123], and (c) [011] austenite crystal directions up to 200 MPa in $\text{Ni}_{54}\text{Fe}_{19}\text{Ga}_{27}$ shape memory alloy.

volumetric energy dissipation, has been labeled as E_{irr} and will be used in further discussions. Interestingly, although the second stage transformation was not fully initiated in the [011] direction shown in Figure 2c, an increased energy dissipation was observed in the stress–strain response when loaded to 200 MPa compared to the other two loading directions in Figures 2a and b. This was due to the gradual onset of the second stage transformation in the [011] orientation as seen in Figure 2c.

According to the data in both Figures 1 and 2, the [123] loading direction exhibited a total transformation strain, ϵ_{tr} , of 3.1% and the [001] direction, a ϵ_{tr} of 4.9%. ϵ_{tr} is depicted on the stress–strain curve in Figure 2b and is the strain produced between the austenite and martensite transformation between the critical stresses σ^{M_s} and σ^{M_f} . The total transformation strains achieved in the [011] direction, from Figure 1, were nearly 3.0% and 1.8 % for each of the successive stress-induced transformations, L₁ austenite to 14M martensite and 14M to L₁₀ martensite, respectively. In total, the cumulative ϵ_{tr} in the [011] was nearly equal to that in the [001], but the [011] demonstrated a multistep transformation and significantly larger cumulative mechanical hysteresis. ϵ_{tr} and elastic modulus in the austenite phase, E_A , for each loading direction at temperature A_f are also determined from the slope of the linear elastic response of austenite and tabulated in Table 1.

The critical transformation stresses were extracted from the forward transformations from the isothermal superelastic tests, like those shown in Figure 2, to generate critical stress – temperature phase diagrams. **Figure 3** contains the critical-stress temperature phase diagram for the [011] austenite direction for

both forward and reverse transformations of the A to M1 and M1 to A transformations and the forward transformation phase diagram of the second stage M1 to M2. On the other hand, the inset shows the slope of the critical stress – temperature phase diagram, or Clausius–Clapeyron (Cs–Cl) slopes, for only the forward transformation in each loading direction when loaded to 200 MPa. Slopes were measured to be 3, 5.6, 4.9, and -0.54 MPa K^{-1} for the [001], [123], [011]^{A–M1}, and [011]^{M1–M2} phase transformations, respectively. Stress–strain data showing the onset of the second-stage transformation in the [011] direction was omitted in the inset for clarity and to keep consistency between loading among the three tested directions.

3.2. Martensitic Transformation Entropy Change

For a single isothermal σ – ϵ curve at the A_f temperature, the entropy change of the SMA can be computed with the Clausius–Clapeyron (Cs^{–1}Cl) equation. The Cs^{–1}Cl expression is

$$-\Delta S^{A \rightarrow M} = \frac{\epsilon_{\text{tr}}}{\rho} \frac{d\sigma^{M_s}}{dT}, \quad (13)$$

where $\Delta S^{A \rightarrow M}$ is the difference in entropy between A and M phases, ϵ_{tr} is the transformation strain, and $\frac{d\sigma^{M_s}}{dT}$ is known as the Clausius–Clapeyron slope, i.e., the slope of the critical stress–temperature phase diagram shown in Figure 3 inset. Equation (13) only provides the entropy difference of the austenite and martensite phases at some temperature and neglects any contribution to the entropy change from linear elastic loading of the austenite or martensite phases.

The entropy change of the martensitic phase transformation was computed for each loading direction using Eq. (13) with the data in Tables 1 and 2 and was listed in Table 2. Table 2 also

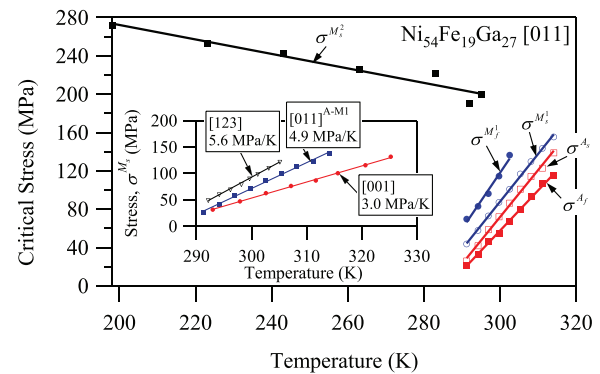


Figure 3. The critical transformation stress versus temperature phase diagram for the forward and reverse transformations in the [011] austenite direction in $\text{Ni}_{54}\text{Fe}_{19}\text{Ga}_{27}$. The critical transformation stress versus temperature phase diagrams for the forward transformations in the [001], [123], and [011] are depicted in the inset.

Table 2. Calculated stress-induced martensite-to-austenite or Martensite 2–1 phase transformation entropy changes, $\Delta S^{A \rightarrow M}$, of the single crystalline $\text{Ni}_{54}\text{Fe}_{19}\text{Ga}_{27}$ shape memory alloy, together with the slope of the stress versus temperature phase diagram, $d\sigma^{Ms}/dT$, from Figure 1b. Data was used to compute $\Delta S^{A \rightarrow M}$ using Eq. (13). The required stress is the critical stress for the onset of stress-induced martensitic transformation, which is the minimum stress required to attain the calculated entropy change for the elasto-caloric effect.

Crystal direction	$d\sigma^{Ms}/dT$ (MPa/K)	$\Delta S^{A \rightarrow M}$ (J/kgK)	$\sigma^{Ms} _{T=A_f}$ (MPa)
[001]	3.04	−19.1	19.5
[123]	5.63	−22.2	41.9
[011]	4.97 ^{a)}	−19.1 ^{a)}	35.2 ^{a)}
	−0.54 ^{b)}	1.3	190 ^{b)}

^{a)} ϵ_{tr} First stage martensitic transformation (L2₁ to 14M martensite).

^{b)} Second stage martensitic transformation (14M to L1₀ martensite).

includes $\frac{d\sigma^{Ms}}{dT}$ values from Figure 3 inset and the critical stress for the forward martensitic transformation. As shown in the data in Table 2, the [001] and [011]^{A–M1} directions exhibited nearly the same entropy change of $-19 \text{ J kg}^{-1} \text{ K}^{-1}$, however, each direction required a different magnitude of stress to achieve the entropy change. Interestingly, the [011] loading direction exhibited a negative entropy change of $-1.24 \text{ J kg}^{-1} \text{ K}^{-1}$ upon removing the mechanical load from the L1₀ (Martensite 2) to 14M (Martensite 1). Upon further unloading, a positive entropy change of $19 \text{ J kg}^{-1} \text{ K}^{-1}$ was generated by the 14M (Martensite 1) to austenite transformation. The small variations in transformation entropy change between these samples was not unexpected and was attributed to experimental temperature uncertainty and slight compositional variations between the NiFeGa single crystals. It is important to note that if the [011] was fully transformed to Martensite 2 with mechanical stresses exceeding 300 MPa, removing the mechanical load would have produced entropy changes from both M2 to M1 and M1 to austenite. As the M1–M2 transformation produces entropy changes opposite in sign to those created by the M1 to A, the overall entropy change would be reduced. Therefore, loading beyond 200 MPa in the [011] reduces the ECE.

3.3. Total Superelastic Elastocaloric Effect

A series of isothermal superelastic unloading curves from 200 MPa were collected along the [001], [123], and [011] directions of the NiFeGa single crystals and the results are shown in Figure 4a–c. In Figure 4a, the austenite phase in the [001] loading direction was found to exhibit a slight increase in stiffness (about 0.8 GPa) as the test temperatures increased beyond A_f up to 353 K. The austenite phase in other crystal loading directions did not show a significant change in E_A with increasing test temperature. Since the samples were mechanically loaded to 200 MPa, the ϵ_{tr} in each orientation appeared to decrease with increasing temperature. This was a byproduct of both a temperature dependent transformation strain and loading the material only to 200 MPa. The [011] direction exhibited a slight increase in ϵ_{tr} with increasing temperature above 291 K, but then started to decrease like the other loading directions as it

was only loaded to 200 MPa. This was attributed to the onset of the M1 \leftrightarrow M2 transformation observed in the [011] direction shown in Figure 1.

Using the isothermal superelastic curves, Eq. (12) was employed to determine the total stress induced entropy change by releasing the mechanical load from an initial condition of

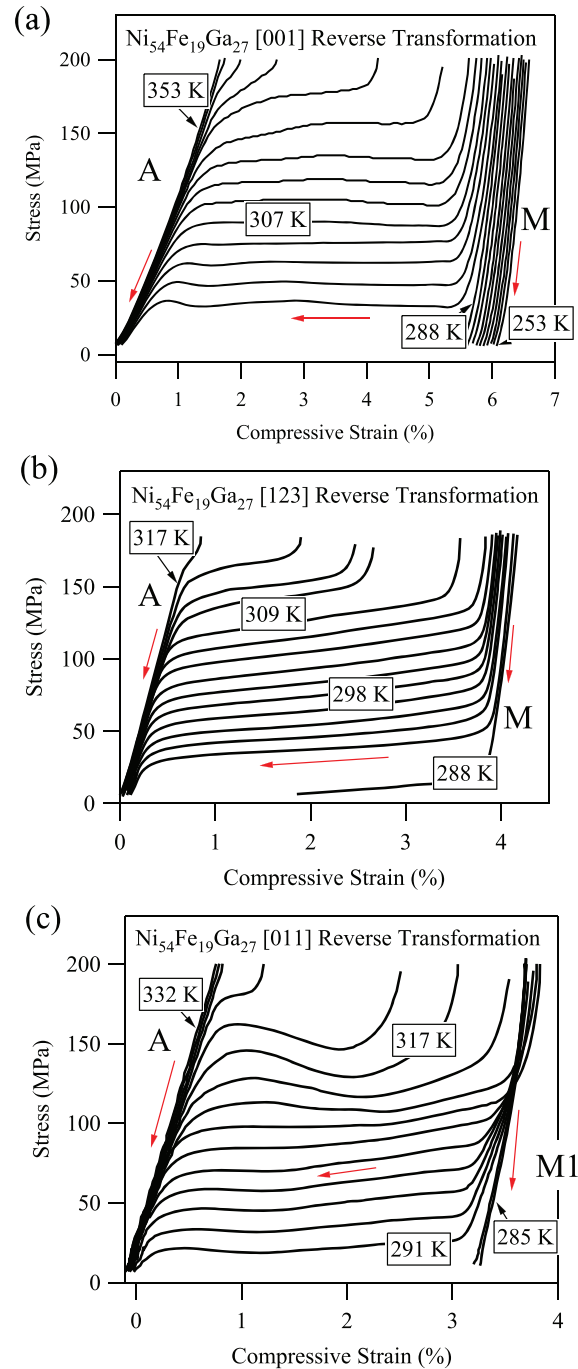


Figure 4. Unloading curves in the superelastic response of the $\text{Ni}_{54}\text{Fe}_{19}\text{Ga}_{27}$ single crystalline compression samples tested along the [001] (a), [123] (b), and [011] (c) directions at temperatures from 253 to 353 K in increments of about 3 K under 0–200 MPa.

200 MPa to zero in each loading direction. This resulted in a positive entropy change and a cooling effect. $\Delta S - T$ curves are shown in Figure 5a–c for the [001], [123], and [011] loading directions, respectively. The values for ΔS in the ΔS versus T curves describe the cumulative entropy change from superelastic unloading. This includes the ECE from unloading the martensite phase, the phase transformation (also computed with the Cs-Cl equation), and unloading the austenite phase. Furthermore, the stress–strain curves for mechanical loading were independently analyzed to determine the ECE heating effect, as represented by the negative entropy changes in the same figures. In theory, the forward and reverse transformation entropy changes should be equal and opposite in sign. Interestingly, the ΔS versus T curves demonstrate that the ΔS slightly increases or decreases with temperature along the plateau of the observed curve. Error bars on the reverse transformation entropy change curves are depicted and were computed by experimental uncertainty mentioned, earlier.

The [001] sample exhibited an average positive entropy change of $17.5 \text{ J kg}^{-1} \text{ K}^{-1}$ (Figure 5a) under superelastic unloading from 5.5% strain within the temperature range of 290–330 K, whereas the [123] and [011] loading directions exhibited average entropy changes of $20.6 \text{ J kg}^{-1} \text{ K}^{-1}$ and $17.7 \text{ J kg}^{-1} \text{ K}^{-1}$ with superelastic unloading from 4% to 3.5%, respectively. Average entropy changes under the maximum strain are indicated on $\Delta S - T$ plots as dashed lines. It is interesting to note the magnitude of temperature intervals where these entropy changes were produced. In the [001] direction, the maximal ΔS could be produced across a range of 45 K, whereas in the [123] the maximal ΔS is achieved across a narrow temperature interval of only 20 K. The [011] loading direction demonstrated that the maximal ΔS could be achieved across a temperature interval of 30 K.

Comparing the magnitude of the average entropy change in Figure 5a–c, with those computed in Table 2 from the Cs-Cl relation, it is evident that the linear elastic contribution to the ECE in NiFeGa single crystals was marginal, but the temperature dependent transformation strain may be significant (see ΔS versus T for the [011] orientation). The entropy change computed for the martensitic transformation with Eq. (13) was labeled on each figure (see 5a–c) by an arrow for comparison against the average. For example, entropy change values computed with Eq. (13) in Table 2 were found to be 19.1, 19.1, and $22.2 \text{ J kg}^{-1} \text{ K}^{-1}$ for the [001], [011], and [123] loading directions, respectively. The difference between the average $\Delta S - T$ curves at the maximum superelastic strain and the entropy change computed with the Cs-Cl equation in Table 2 is +1.6, +1.4, and $+1.6 \text{ J kg}^{-1} \text{ K}^{-1}$, respectively. These very small differences were attributed to sample to sample variation and experimental uncertainty.

3.4. Thermodynamic Losses through Mechanical Hysteresis

In general, applying a mechanical load to a single phase material will cause elastocaloric heating as indicated by the negative entropy change in Eq. (11). Removing the mechanical load results in cooling through the equal and opposite linear elastic ECE without noticeable thermodynamic loss. Across martensitic transformations, on the other hand, thermodynamic loss is produced by the martensitic transformation. This is produced

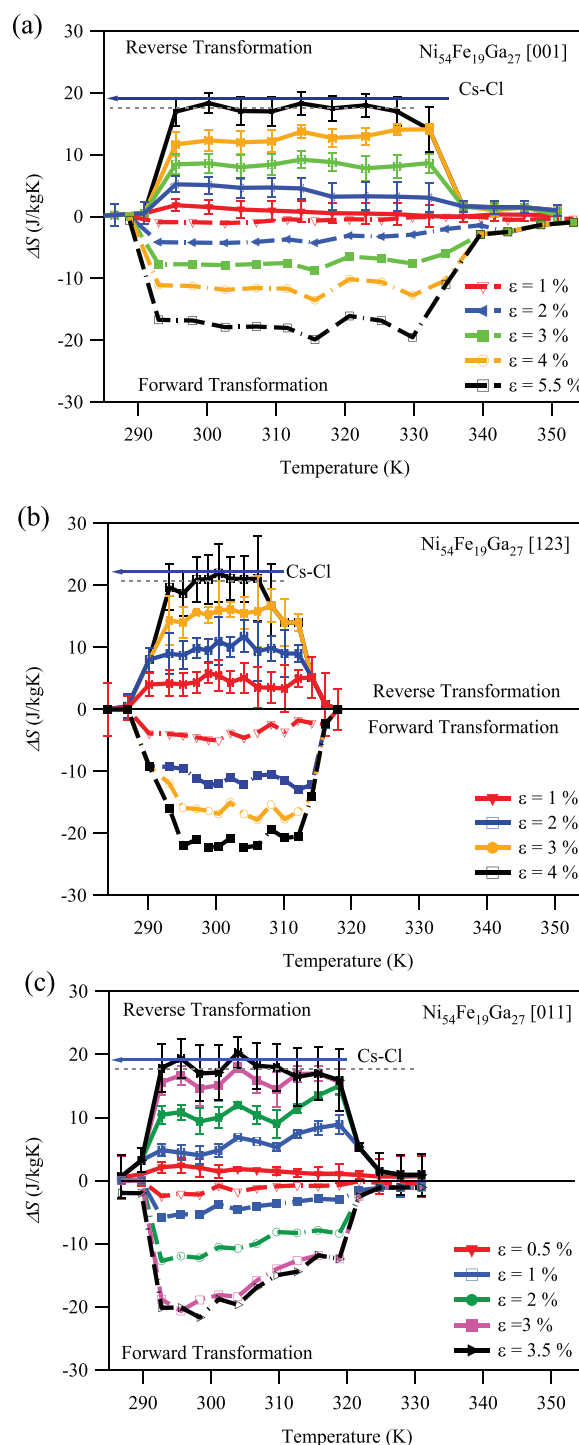


Figure 5. Entropy change versus temperature (ECE) curves as a function of superelastic strain (ϵ) in the $\text{Ni}_{54}\text{Fe}_{19}\text{Ga}_{27}$ single crystalline compression samples tested along the [001] (a), [123] (b), and [011] (c) austenite directions at temperatures from 253 to 353 K in increments of about 3 K under 0–200 MPa. The entropy change computed only for the martensitic phase transformation using Eq. (13) is labeled in the figures as Cs-Cl. The dashed line represents the average entropy change across the operating temperature interval at the maximum indicated strain.

from internal friction and irreversible microstructural defect generation.^[49] Energy dissipation, or hysteresis loss, E_{irr} (J/kg), was computed from the isothermal superelastic loading-unloading curves in Figure 4a–c by the area of the stress

hysteresis, i.e., $E_{\text{irr}} = \frac{1}{\rho} \left(\int_0^{\epsilon} \sigma^{\text{forward}} d\epsilon - \int_0^{\epsilon} \sigma^{\text{reverse}} d\epsilon \right)$, where ρ

was defined as mass density (kg m^{-3}). E_{irr} was computed in each loading direction at each isothermal test temperature up to the superelastic ϵ corresponding to those on the $\Delta S - T$ curves. $E_{\text{irr}} - T$ diagrams are shown in Figure 6a–c for the [001], [123], and [011] austenite crystal loading directions, respectively. On average, the maximum E_{irr} was determined to be 150, 132, 190, and 272 J kg^{-1} for the [001], [123], [011]^{A–M1}, [011]^{M1–M2} transformations, respectively. Note that these maximums were reached at different superelastic strain levels for each orientation. Close observation of the $E_{\text{irr}} - T$ diagrams indicates a minor

temperature dependence of hysteretic losses in each loading direction probably due to the temperature dependent transformation strain. The E_{irr} in the [001] direction, for example, appears to slightly increase as temperature decreases. In the [123] direction, E_{irr} remains fairly constant across the entire temperature interval, whereas in the [011] direction, E_{irr} appears to decrease with decreasing temperature when loaded to strains above 2%.

Figure 6c shows E_{irr} in the [011] direction, and at 291 K, hysteresis losses were computed from the superelastic loading in the inset up to 350 MPa. Strains labeled as “1,” “2,” and “3” correspond to 4%, 5%, and 5.5% superelastic loading for stresses up to 200, 250, and 280 MPa, respectively. The increase in hysteresis loss exhibited a major jump, from 4% strain to 5% strain, of 173 J kg^{-1} . Furthermore, completing the M1 to M2 transformation by applying stresses up to 350 MPa demonstrated that the second-stage transformation in the [011]

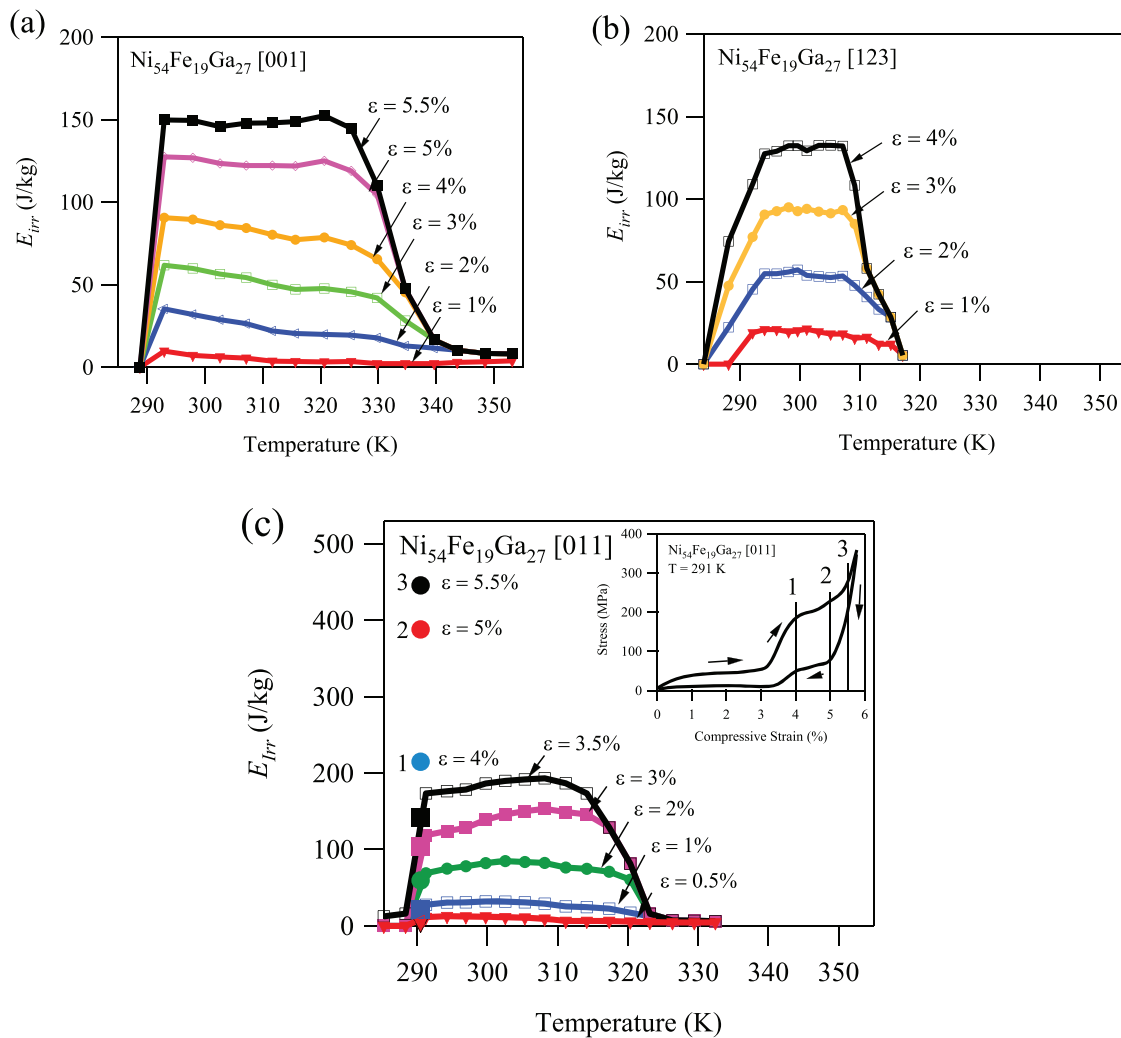


Figure 6. Hysteresis loss versus temperature curves as a function of superelastic strain (ϵ) in the $\text{Ni}_{54}\text{Fe}_{19}\text{Ga}_{27}$ single crystalline compression samples tested along the [001] (a), [123] (b), and [011] (c) directions at temperatures from 253 to 353 K in increments of about 3 K under 0–200 MPa. In (c) the hysteresis loss is presented at 291 K for strains up to 5.5% (at 4%, 5%, and 5.5% strain levels) and stresses up to 350 MPa as shown by the stress–strain behavior in the inset. Driving the multi-step transformation produces a hysteresis loss of 445 J/kg at 5.5% strain.

direction generated 272 J kg^{-1} more loss than that for the first-stage transformation (173 J kg^{-1}). The second-stage transformation was found to generate nearly double the loss of the first-stage transformation. The hysteresis loss at 291 K up to 5.5% strain will be used later to compute the relative cooling power in the [011] direction when loading above 200 MPa.

Since mechanical hysteresis indicated thermodynamic loss through friction (heat), it was assumed that entropy was produced by the transformation process. The entropy production, S_{prod} was approximated from the isothermal tests by dividing E_{irr} by 2, and then dividing by the test temperature. Since the cooling effect occurred on unloading the SMA, we assumed only half of the E_{irr} contributed to S_{prod} . The entropy production was then approximated as $-S_{\text{prod}} = E_{\text{irr}}/(2 \cdot T)$ and was assumed to always be negative in sign no matter the loading direction is, i.e., friction caused heat in forward or reverse martensitic transformations.

Clearly, the [011] direction exhibited a much larger stress hysteresis and thermodynamic loss than the [001] and [123] directions, as shown in the superelastic responses of Figure 1, which could be inhibitive in the ECE applications. As listed above, the second-stage transformation in the [011] required mechanical loading up to 258 MPa. This was the highest magnitude of stress at the A_f temperature to transform all of the samples under investigation. However, Table 2 demonstrates that an equivalent entropy change could be produced by the [001] by applying and releasing a lower magnitude of mechanical stress. The entropy production caused by the second-stage transformation from Martensite 2 to Martensite 1 in the [011] direction was $-0.47 \text{ J kg}^{-1} \text{ K}^{-1}$ and the Martensite 2 to Martensite 1 transformation entropy change was computed to be $-1.24 \text{ J kg}^{-1} \text{ K}^{-1}$. As entropy changes are additive, unloading across the second-stage transformation in the [011] direction was expected to generate a heating effect, rather than a cooling effect from the latent heat, and cumulative entropy change of $-1.71 \text{ J kg}^{-1} \text{ K}^{-1}$. During the Martensite 1 to austenite transformation, on the other hand, entropy production was only $-0.33 \text{ J kg}^{-1} \text{ K}^{-1}$ and an entropy change of $19.1 \text{ J kg}^{-1} \text{ K}^{-1}$ was computed with the Cs-Cl equation indicating a cumulative cooling reaction. This implies a total cooling effect was generated by removing the mechanical load across the first-stage martensitic transformation causing a ΔS of $17.0 \text{ J kg}^{-1} \text{ K}^{-1}$.

Considering that the second-stage martensitic transformation in the [011] direction exhibited the largest thermodynamic loss (see Figure 6c) and an entropy change opposing that of the first-stage stress-induced transformation (see Table 2), it was apparently inhibitive to trigger the second-stage martensitic transformation, M2 to M1, in the [011] direction. Thus, this stress level was intended to avoid the second-stage transformation in the [011] direction, but still provide enough stress to complete the martensitic transformation at a wide range of temperatures in all of the tested crystal directions.

3.5. Strain Dependent Relative Cooling Power

An interesting feature of the strain-dependent $\Delta S - T$ curves derived from the Helmholtz free energy was the signature plateau in ΔS . These curves expanded upward in entropy change with increasing superelastic strain, rather than to the left or right

in the temperature axis when compared to MCE studies where data was analyzed with the Gibbs free energy potential. Thus, our ECE curves were ideal for computing the relative cooling power (RCP) defined, here, as^[41]

$$\text{RCP} \approx \Delta S_{\text{Total}}^{\text{Max}}(\varepsilon) \cdot \Delta T_{\text{fwhm}} - S_{\text{prod}}^{\text{Max}}(\varepsilon) \cdot \Delta T_{\text{fwhm}}. \quad (14)$$

In Equation (14), the RCP is computed from ECE cooling curves (positive entropy change) by multiplying the maximum entropy change at a given strain with the temperature interval (ΔT) at full width half maximum (fwhm) where the entropy change was observed. Thermodynamic losses from hysteresis were then removed by subtracting the product of the maximum entropy production with the same temperature interval. Each strain dependent entropy change vs. temperature data was used to compute the RCP in Eq. (14) and were plotted in Figure 7 as a function of total superelastic compressive strain.

When unloaded from 200 MPa, the [001] direction exhibited the largest SE strain, followed by the [123] and then the [011]. The [001] direction was characterized by the largest RCP, of 738 J kg^{-1} at 5.5% strain, followed by the [011] of 585 J kg^{-1} at 3.5% strain, and the [123] of 477 J kg^{-1} at 4% strain. Clearly, the [001] direction exhibited the largest RCP, the lowest E_A , lowest Cs-Cl slope, and highest ε compared to the [123] and [011] directions under 200 MPa. As the Cs-Cl slope is the lowest in the [001] direction, compared to the other loading directions, the entropy change versus temperature diagrams exhibited the widest ΔT_{fwhm} of 45 K. This is mainly because of the lowest Cs-Cl slope and the fact that in many ordered SMAs, including Heusler SMAs, the [001] direction is the least prone to transformation induced plasticity and thus, shows the best reversibility among other orientations, leading to the largest superelastic temperature window. Interestingly, the stress-induced martensitic transformation generated an entropy change that was nearly equal in each loading direction (see Table 2), however, the crystallographic anisotropy and behavior in the [001] is favorable to maximize the RCP in NiFeGa through the width of the operating temperature and small mechanical hysteresis of 16 MPa. However, when exercised to only 3% strain, the [001]

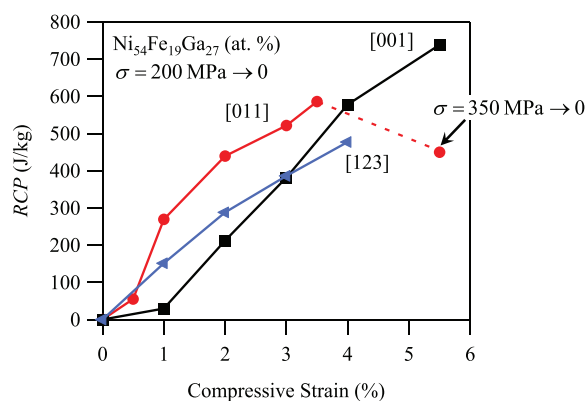


Figure 7. The relative cooling power (RCP) as a function of superelastic compressive strain in the [001], [123], and [011] $\text{Ni}_{54}\text{Fe}_{19}\text{Ga}_{27}$ austenite crystal directions for loading up to 200 MPa. The second stage transformation in the [011] loading direction, driven with 350 MPa, is observed to decrease the RCP by 135 J kg^{-1} .

showed the smallest RCP due to the incomplete martensitic transformation (i.e., larger transformation strain along the [001] direction), the lowest elastic modulus and thus, the highest elastic strain, which did not contribute much to the RCP. It was shown in Figures 2 and 4a that, for the [001] direction, nearly 1% strain at all test temperatures was generated by linear elasticity in the austenite phase and not the phase transformation. Thus, the RCP of the [001] is comparatively low up to 1% strain.

On the other hand, the [011] orientation exhibited a larger RCP for most strain levels by unloading from 200 MPa. This was attributed to the relatively high Cs-Cl slope, small transformation strain, and high E_A of the [011] orientation. This data suggests some optimum materials properties might exist that will maximize the RCP in SMAs. The operating temperature window of the [011] orientation to achieve the transformation entropy change was determined to be 30 K at full-width-half-maximum. Loading the [011] direction beyond the primary M1-A martensitic transformation will have caused a decrease in the RCP by decreasing the entropy change at high strain levels. For example, the RCP (5.5%) was computed and plotted in Figure 7 for the [011] assuming loading/unloading from 350 MPa with E_{irr} data from Figure 6c inset. The data point at 5.5% strain in the [011] RCP curve was computed assuming a $\Delta T_{fwhm} = 30$ K, $\Delta S_{Total}^{Max}(5.5\%) = 17 \text{ J kg}^{-1} \text{ K}^{-1} - 1.24 \text{ J kg}^{-1} \text{ K}^{-1} = 15.8 \text{ J kg}^{-1} \text{ K}^{-1}$ and $S_{prod}^{Max}(5.5\%) = \frac{445 \text{ J kg}^{-1}}{(2.291 \text{ K})} = 0.76 \text{ J kg}^{-1} \text{ K}^{-1}$. The Martensite 2 to Martensite 1 transformation was responsible for $-1.24 \text{ J kg}^{-1} \text{ K}^{-1}$ and the Martensite 1 to austenite transformation was responsible for $17 \text{ J kg}^{-1} \text{ K}^{-1}$. Thus, the cumulative entropy change was $15.8 \text{ J kg}^{-1} \text{ K}^{-1}$. Similarly, the cumulative hysteresis loss generated by loading up the sample to 5.5% strain was 445 J kg^{-1} at 291 K as shown in Figure 6c. Loading beyond 200 MPa, and driving the transformation to Martensite 2 reduces the RCP in the [011] direction to 449 J kg^{-1} from 585 J kg^{-1} . In other words, driving the second transformation from Martensite 2 to Martensite 1 reduced the RCP by 135 J kg^{-1} .

Finally, the [123] exhibited the smallest RCP of 477 J kg^{-1} when loaded to maximal strain under 200 MPa, but was typically higher than the [001] direction when loaded to smaller strains. The difference between the [123] and [001] RCP curves was attributed, again, to the steep Cs-Cl slope in Figure 3 and a harder austenite phase (larger E_A). The [123] orientation did not reach a high RCP due to the steep Cs-Cl slope that limits the operating temperature window (20 K) when loaded to 200 MPa. Both the [123] and [011] loading directions are characterized by similar RCP at $\varepsilon < 0.5\%$ as E_A was also similar in both austenite loading directions. Clearly, loading the [123] direction to higher stresses would provide a means of increasing its RCP to values comparable with the [001] as the ΔT_{fwhm} would continue to increase at a rate controlled by the Cs-Cl slope. As the Cs-Cl slope is lower in the [123] direction compared to the [001] direction, we expect the [001] loading direction to remain the orientation lending the highest RCP for any given maximal stress.

4. Summary and Conclusions

In this study, $\text{Ni}_{54}\text{Fe}_{19}\text{Ga}_{27}$ shape memory alloy single crystals were studied during loading along the [001], [123], and [011]

austenite crystal directions to determine the elasto-caloric effects during the austenite to martensite forward and reverse transformations to reveal the orientation dependence of the elasto-caloric effect and relative cooling power (RCP). The Helmholtz free energy potential was employed to predict the entropy changes from the superelastic responses for these crystal directions. Each loading direction exhibited a stress-induced martensitic transformation that was recoverable upon mechanical unloading. Unloading stress-strain curves were used to compute the elasto-caloric effect and, thus, unloading curves lend the ability to compute the cumulative entropy changes of the martensite and austenite phases and the martensitic transformation.

Although the entropy change generated by the martensitic transformation was found to be nearly equivalent in each crystal direction, we found that the RCP was orientation dependent. The crystal anisotropy in the austenite modulus of elasticity as well as the differences in mechanical hysteresis between the austenite crystal directions appeared to play pivotal roles in the RCP. It was found that driving the second stage martensitic transformation in the [011] crystal direction ultimately reduced its RCP by 135 J kg^{-1} compared to only loading to 200 MPa and driving the first transformation. The [001] loading direction exhibited the overall highest RCP of 738 J kg^{-1} at 5.5% strain by unloading from 200 MPa, whereas the [123] and [011] directions were characterized by RCPs of 477 J kg^{-1} and 585 J kg^{-1} , respectively. If the single crystals were loaded to higher mechanical stresses, i.e., >200 MPa, the [001] direction operating temperature window would still be the largest and [123] the smallest. This was a byproduct of the differences in the slopes of the Clausius-Clapeyron relations. Additionally, the RCP in the [011] direction would quickly drop if the SMA was loaded beyond 200 MPa (or 3.5% strain) due to the behavior of the second-stage 14M and $L1_0$ martensitic transformation. Not only does this transformation exhibit the largest hysteretic losses of 272 J kg^{-1} , but it produces a negative entropy change of $-1.24 \text{ J kg}^{-1} \text{ K}^{-1}$. The [001] loading direction exhibited the softest austenite phase with an elastic modulus of 7.4 GPa and the lowest Clausius-Clapeyron slope of 3 MPa K^{-1} , thus maximizing the operating temperature window for elasto-caloric effect (45 K) when loaded to 200 MPa. However, the soft austenite phase resulted in a comparatively low RCP when operating under strains below 0.5% when compared to the [123] and [011] austenite crystal directions.

Acknowledgements

This work was supported by the U.S. National Science Foundation, Division of Materials Research, Metals and Metallic Nanostructures Program, Grant No. 1508634. Prof. Y. I. Chumlyakov acknowledges the support of Russian Ministry of Education and Science project 16.6554.2017/6.7 and by The Tomsk State University Academic D.I. Fund Program project 8.140.2017.

Conflict of Interest

The authors declare no conflict of interest.

Keywords

elastocaloric effect, ferrocaloric materials, magnetic shape memory alloys, relative cooling power, superelasticity

Received: August 13, 2017

Revised: November 3, 2017

Published online:

References

- [1] D. C. Lagoudas, *Shape Memory Alloys: Modeling and Engineering Applications*. Springer Media L.L.C., New York, NY, US **2008**, pp. 29–40
- [2] J. Ma, I. Karaman, *Science* **2010**, *327*, 1468.
- [3] B. Kockar, K. C. Atli, J. Ma, M. Haouaoui, I. Karaman, M. Nagasako, R. Kainuma, *Acta Mater.* **2010**, *58*, 6411.
- [4] D. J. Leo, *Engineering Analysis of Smart Material Systems*. Wiley & Sons, Inc., Hoboken, NJ, US **2008**.
- [5] J. Ma, I. Karaman, R. D. Noebe, *Int. Mater. Rev.* **2010**, *55*, 257.
- [6] V. K. Pecharsky, K. A. Gschneidner, Jr., O. Pecharsky, A. M. Tishin, *Phys. Rev. B* **2001**, *64B*, 144406.
- [7] N. M. Bruno, Y. J. Huang, C. L. Dennis, J. G. Li, R. D. Shull, J. H. Ross, Y. I. Chumlyakov, I. Karaman, *J. Appl. Phys.* **2016**, *120*, 075101.
- [8] T. D. Brown, I. Karaman, P. J. Shamberger, *Mater. Res. Express* **2016**, *3*, 074001.
- [9] J.-H. Chen, N. M. Bruno, I. Karaman, Y. J. Huang, J. G. Li, J. H. Ross, *Acta Mater.* **2016**, *105*, 176.
- [10] B. Emre, N. M. Bruno, S. Y. Emre, I. Karaman, *Appl. Phys. Lett.* **2014**, *105*, 231910.
- [11] J.-H. Chen, N. M. Bruno, I. Karaman, Y. J. Huang, J. Li, J. H. Ross, *J. Appl. Phys.* **2014**, *116*, 203901.
- [12] A. Planes, L. Manosa, M. Acet, *J. Phys.: Condens. Matter* **2009**, *21*, 233201.
- [13] J. Liu, T. Gottschall, K. P. Skokov, J. D. Moore, O. Gutfleisch, *Nature Mater.* **2012**, *11*, 620.
- [14] T. Krenke, E. Duman, M. Acet, E. F. Wassermann, X. Moya, L. Manosa, A. Planes, E. Suard, B. Ouladdiaf, *Phys. Rev. B* **2007**, *75B*, 104414.
- [15] M. Pasquale, C. P. Sasso, L. H. Lewis, L. Giudici, T. Lograsso, D. Schlagel, *Phys. Rev. B* **2005**, *72B*, 094435.
- [16] S. Faehler, U. K. Roessler, O. Kastner, J. Eckert, G. Eggeler, H. Emmerich, P. Entel, S. Muller, E. Quandt, K. Albe, *Adv. Eng. Mater.* **2012**, *14*, 10.
- [17] L. Mañosa, D. González-Alonso, A. Planes, E. Bonnot, M. Barrio, J.-L. Tamarit, S. Aksoy, M. Acet, *Nature Mater.* **2010**, *9*, 478.
- [18] E. Stern-Taulats, A. Planes, P. Lloveras, M. Barrio, J. L. Tamarit, S. Pramanick, S. Majumdar, S. Yuce, B. Emre, C. Frontera, L. Manosa, *Acta Mater.* **2015**, *96*, 324.
- [19] J. Cui, Y. Wu, J. Muehlbauer, Y. Hwang, R. Radermacher, S. Fackler, M. Wuttig, I. Takeuchi, *Appl. Phys. Lett.* **2012**, *101*, 073904.
- [20] E. Pieczyska, J. Dutkiewicz, F. Masdeu, J. Luckner, R. Maciak, *Arch. Metall. Mater.* **2011**, *56*, 401.
- [21] Y. J. Huang, Q. D. Hu, N. M. Bruno, J.-H. Chen, I. Karaman, J. H. Ross, J. G. Li, *Scr. Mater.* **2015**, *105*, 42.
- [22] E. Bonnot, R. Romero, L. Manosa, E. Vives, A. Planes, *Phys. Rev. Lett.* **2008**, *100*, 125901.
- [23] N. M. Bruno, S. Wang, I. Karaman, Y. I. Chumlyakov, *Sci. Rep.* **2017**, *7*, 40434.
- [24] Y. Wu, E. Ertekin, H. Sehitoglu, *Acta Mater.* **2017**, *135*, 158.
- [25] Y. Xu, B. Lu, W. Sun, A. Yan, J. Liu, *Appl. Phys. Lett.* **2015**, *106*, 201903.
- [26] L. Manosa, A. Planes, E. Vives, E. Bonnot, R. Romero, *Funct. Mater. Lett.* **2009**, *2*, 73.
- [27] D. E. Soto-Parra, E. Vives, D. Gonzales-Alonso, L. Manosa, A. Planes, R. Romero, J. A. Matutes-Aquino, R. A. Ochoa-Gamboa, H. Flores-Zuniga, *Appl. Phys. Lett.* **2010**, *96*, 071912.
- [28] P. O. Castillo-Villa, De. E. Soto-Parra, J. A. Matutes-Aquino, R. A. Ochoa-Gamboa, A. Planes, L. Manosa, D. Gonzalez-Alonso, M. Stipcich, R. Romero, D. Rios-Jara, H. Flores-Zuniga, *Phys. Rev. B* **2011**, *83B*, 174109.
- [29] P. O. Castillo-Villa, L. Manosa, A. Planes, D. E. Soto-Parra, J. L. Sanchez-Llamazares, H. Flores-Zuniga, C. Frontera, *J. Appl. Phys.* **2013**, *113*, 053506.
- [30] R. F. Hamilton, C. Efstathiou, H. Sehitoglu, Y. Chumlyakov, *Scr. Mater.* **2006**, *54*, 465.
- [31] E. E. Timofeeva, E. Y. Panchenko, Y. I. Chumlyakov, H. Maier, *Russ. J. Phys.* **2012**, *54*, 1427.
- [32] C. Efstathiou, H. Shitoglu, J. Carroll, J. Lambros, H. J. Maier, *Acta Mater.* **2008**, *56*, 3791.
- [33] Y. I. Chumlyakov, I. V. Kireeva, E. Y. Panchenko, E. E. Timofeeva, Z. V. Pobedennaya, S. V. Chusov, I. Karaman, H. Maier, E. Cesari, V. A. Kirillov, *Russ. J. Phys.* **2008**, *51*, 1016.
- [34] E. E. Timofeeva, E. Y. Panchenko, Y. I. Chumlyakov, A. I. Tagiltsev, *Russ. J. Phys.* **2015**, *57*, 1268.
- [35] Y. I. Chumlyakov, I. V. Kireeva, E. Y. Panchenko, E. E. Timofeeva, Z. V. Pobedennaya, S. V. Chusov, I. Karaman, H. J. Maier, E. Cesari, V. A. Kirillov, *Russ. J. Phys.* **2008**, *51*, 1016.
- [36] E. Panchenko, Y. I. Chumlyakov, H. J. Maier, E. Timofeeva, I. Karaman, *Intermetallics* **2010**, *18*, 2458.
- [37] K. Oikawa, T. Ota, T. Ohmori, Y. Tanaka, H. Morito, A. Fujita, R. Kainuma, K. Fukamichi, K. Ishida, *Appl. Phys. Lett.* **2003**, *81*, 5201.
- [38] Y. Sutou, N. Kamiya, T. Omori, R. Kainuma, K. Ishida, K. Oikawa, *Appl. Phys. Lett.* **2004**, *84*, 1275.
- [39] R. F. Hamilton, H. Sehitoglu, C. Efstathiou, H. J. Maier, *Scr. Mater.* **2007**, *57*, 497.
- [40] J. Ma, B. Kockar, A. Evirgen, I. Karaman, Z. P. Luo, Y. I. Chumlyakov, *Acta Mater.* **2012**, *60*, 2186.
- [41] N. M. Bruno, C. Yegin, I. Karaman, J.-H. Chen, J. H. Ross, J. Liu, J. G. Li, *Acta Mater.* **2014**, *74*, 66.
- [42] M. K. Chattopadhyay, V. K. Sharma, S. B. Roy, *Appl. Phys. Lett.* **2008**, *92*, 022503.
- [43] A. Chauhan, S. Patel, R. Vaish, C. R. Bowen, *MRS Energy Sustainability* **2015**, *2*, e16.
- [44] G. J. Liu, J. R. Sun, J. Shen, B. Gao, H. W. Zhang, F. X. Hu, B. G. Shen, *Appl. Phys. Lett.* **2007**, *90*, 032507.
- [45] R. Niemann, O. Heczko, L. Shultz, S. Fahler, *Int. J. Refrig.* **2014**, *37*, 281.
- [46] A. Planes, L. Manosa, M. Acet, *J. Phys.: Condens. Matter* **2009**, *21*, 233201.
- [47] R. F. Hamilton, H. Sehitoglu, C. Efstathiou, H. J. Maier, *Acta Mater.* **2007**, *55*, 4867.
- [48] N. Ozdemir, I. Karaman, N. A. Mara, Y. I. Chumlyakov, H. E. Karaca, *Acta Mater.* **2012**, *60*, 5670.
- [49] H. Funakubo, *Precision Machinery and Robotics: Actuators for Control* (Vol. 2). Gordon and Breach Science Publishers, Amsterdam **1991**, pp. 39–60.